Capillary Bridges between Soft Substrates

Jason S. Wexler, Tiara M. Heard, and Howard A. Stone*
Department of Mechanical and Aerospace Engineering, Princeton University, Princeton, New Jersey 08544, USA
(Received 21 October 2013; published 14 February 2014)

A wetting droplet trapped in the thin gap between two elastic bodies will deflect the bodies towards one another. The deformation increases the total capillary adhesion force by increasing the contact radius and narrowing the gap height. For flat droplets, with a large ratio of radius to gap height, the Laplace pressure causes surface deformations that are orders of magnitude larger than those induced by a sessile droplet of the same radius. We present experiments, scalings, and closed-form solutions that describe the deformation. Using variational techniques, we also show that the problem exhibits a bifurcation, where the gap spontaneously closes due to an incremental increase in drop volume.

DOI: 10.1103/PhysRevLett.112.066102 PACS numbers: 68.03.Cd, 46.25.-y, 46.55.+d

Capillary adhesion is a classic example of the strength of surface tension forces; when a drop of wetting liquid bridges a gap separating two nearby surfaces, large normal forces can develop if the gap is very thin [1]. These forces may dominate a wide variety of physical systems, ranging from the stability of granular structures [2] and the adhesion of insects [3] to a glass of cold water stuck to a table. If the adhering objects are soft, the trapped droplet can pull the two surfaces of the gap together as shown in Fig. 1, which increases the adhesion force by magnifying the Laplace pressure and enlarging the contact radius. Previous efforts to understand capillary bridges between elastic materials have focused on interactions between spheres, extending the Hertz theory of contact [4] to include effects of a capillary meniscus [5–7]. We focus on the case of a droplet trapped in a thin gap, and report experiments, scalings, and closed-form solutions for the deformation.

A sessile droplet resting unconstrained on an elastic substrate deforms the solid underneath it by an amount $\mathcal{O}(\gamma/E)$, which is termed the elastocapillary length [8], where γ is the surface tension of the fluid-fluid interface and E is the Young's modulus of the substrate [9–12]. Most everyday liquids have a surface tension on the order of 10−100 mN/m. Therefore, in order for a sessile droplet to deform a solid substrate by even a few microns, the material must be very soft, with a Young's modulus in the range of 10–100 kPa [13–15].

We consider a drop trapped between two elastic surfaces (Fig. 1). A scaling analysis demonstrates that the vertical deformations u_z are orders of magnitude larger for this configuration than for a similarly sized sessile drop. For the case of a sessile drop, the Laplace pressure scales as γ/a, where a is the droplet radius. The pressure is balanced by elastic stresses within the solid $\mathcal{O}(Eu_z/a)$, leading to deformations $\mathcal{O}(\gamma/E)$ as indicated above. However, for a droplet between two surfaces separated by a distance h, as in Fig. 1, the Laplace pressure scales instead as γ/h, while the elastic stress scales as before. Balancing pressure and surface stress leads to deformations $\mathcal{O}(\gamma a/Eh)$, which can be substantial if the droplet is flat ($h \ll a$).

Certain organisms with flexible appendages rely on moisture to form an adhesive capillary bridge to an underlying substrate [16]. The system we are studying is a simplified version of this case, and could bring an understanding to the different forces at play in these complex systems. In addition, our results extend the elastocapillary instability of thin MEMS structures [17] to include high aspect ratio microfluidic or other devices fabricated from flexible (but nonthin) polymeric materials. Microfluidic devices are known to deform at high flow rates [18], but may also be susceptible to deformation in a static configuration due to capillary forces alone. Our study also provides insight into crack propagation in the presence of moisture. Moisture at the tip of a crack can arrest crack growth [19,20], but the effect of moisture at some intermediary location is unknown.

We begin by describing in detail the geometry of our study, as shown in Fig. 1. We specify a cylindrical coordinate system whose origin lies at the center of a circular droplet. The width of the gap approaches h as $r \to \infty$. The liquid-air interface has a surface tension γ

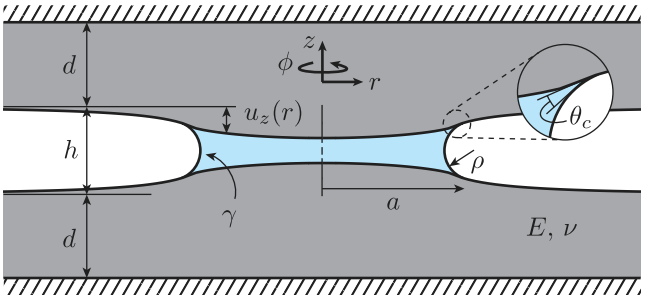

FIG. 1 (color online). Cross section of the axisymmetric geometry, where a droplet bridges two elastic substrates.

and is assumed to wet the solid with a contact angle $\theta_c \approx 0$. We limit our study to small Bond numbers, where gravitational effects are negligible compared to capillary forces. The two solids are identical, with Young's modulus E and Poisson's ratio ν. The vertical deflection of the surface of each substrate in the outward-normal direction is denoted u_z, and for an axisymmetric geometry we have $u_z = u_z(r)$. The radius of the droplet contact line, after the substrates have deformed and the droplet radius has equilibrated, is a. We start with the case of an infinitely thick substrate, and follow with an analysis of substrates with finite thickness d.

Inside the contact radius, the droplet exerts a constant Laplace pressure Δp on the substrate. At the contact line a force per unit length equal to γ pulls on the substrate. In the limit of a very flat droplet, however, the deformation generated by the contact line force is negligible compared to the deformation induced by the Laplace pressure. Thus, the stress boundary condition at the surface of the elastic substrate is

$$\sigma_{zz} = \begin{cases} \Delta p & \text{for } r < a \\ 0 & \text{for } r > a, \end{cases} \tag{1}$$

where the stress is a function of the local strains by the standard linear constitutive relations [21].

In the limit of $d/a \to \infty$, the Navier equations with boundary conditions (1) have a well-known analytical solution [9]. The vertical deformation at the surface is

$$u_z(r) = -\frac{2(1-\nu^2)a\Delta p}{E}\mathcal{I}\left(\frac{r}{a}, \frac{d}{a} \to \infty\right), \tag{2}$$

where

$$\mathcal{I}\left(\frac{r}{a}, \frac{d}{a} \to \infty\right) = \begin{cases} \frac{2}{\pi}E\left(\frac{r}{a}\right) & \text{for } r < a \\ \frac{2r}{\pi a}\left\{E\left(\frac{a}{r}\right) - \left[1 - \left(\frac{a}{r}\right)^2\right]K\left(\frac{a}{r}\right)\right\} & \text{for } r > a\,, \end{cases} \tag{3}$$

and $K(\cdot)$ and $E(\cdot)$ are, respectively, the complete elliptic integrals of the first and second kind. The function $\mathcal{I}(r/a, d/a)$ is dimensionless, and has been introduced to simplify the presentation.

For a substrate with finite thickness, we follow the method of Style and Dufresne [12]. Briefly, the stress and displacement fields are converted to Fourier space using Hankel transform methods. In Fourier space, the deformation is linearly related to the stress by a second-order matrix. We specify the surface stresses given in Eq. (1), and perform the necessary manipulations to obtain a displacement in the form of Eq. (2), but with

$$\mathcal{I}\left(\frac{r}{a}, \frac{d}{a}\right) = \int_0^\infty \frac{1}{s}\frac{[(3-4\nu)\,\sinh(2sd) - 2sd]J_1(sa)J_0(sr)}{5 - 12\nu + 8\nu^2 + 2s^2d^2 + (3-4\nu)\cosh(2sd)}\,ds, \tag{4}$$

where $J_k(\cdot)$ is the kth-order Bessel function of the first kind. It can be shown that Eq. (4) approaches Eq. (3) as $d/a \to \infty$.

The next task is to self-consistently determine the Laplace pressure Δp inside the droplet. We have already specified that the droplet perimeter is circular; this is the equilibrium shape for an ideal system devoid of surface imperfections, gap irregularities, etc. As shown in Fig. 1, the liquid-air interface has two principle radii of curvature, ρ and a [22]. Thus, the Laplace pressure is $\Delta p = \gamma(a^{-1} - \rho^{-1})$, where $\rho = [(h/2) - u_z(a)]\sqrt{1 + (du_z/dr|_{r=a})^2}$.

We substitute this expression into Eq. (2) to determine the deformation for a given droplet size. The equations reveal natural nondimensionalizations for the radial coordinate and deformation, $[r] = a$ and $[u_z] = 4\gamma(1-\nu^2)a/Eh$, which agree with the scaling argument given earlier. Thus, the nondimensional deformation (denoted by a tilde) is

$$\tilde{u}_z(\tilde{r}) = \left(-\frac{h}{2a} + \frac{1}{\beta\left[1 - \frac{8\ell_{\mathrm{EC}}a}{h^2}\tilde{u}_z(1)\right]}\right)\mathcal{I}\left(\tilde{r}, d/a\right), \tag{5}$$

where $\beta = \sqrt{1 + \left(\frac{4\ell_{\mathrm{EC}}}{h}\frac{d\tilde{u}_z}{d\tilde{r}}|_{r=1}\right)^2}$, and $\ell_{\mathrm{EC}} = (1-\nu^2)\gamma/E$ is a modified version of the elastocapillary length introduced earlier.

We have already assumed that $h \ll a$, since this limit produces the most dramatic deformations. Furthermore, we assume that $\ell_{\mathrm{EC}} \ll h$, because otherwise the gap would close with only the slightest amount of moisture. In these limits, Eq. (5) simplifies considerably and becomes

$$\tilde{u}_z(\tilde{r}) = \frac{1}{1 - \Lambda\tilde{u}_z(1)}\mathcal{I}\left(\tilde{r}, \frac{d}{a}\right), \tag{6}$$

with $\Lambda = 8\ell_{\mathrm{EC}}a/h^2$ as the ratio between the expected deformation and the half-height of the gap [23].

We now solve for the deformation at the contact line $\tilde{u}_z(1)$ by evaluating Eq. (6) at $\tilde{r} = 1$. This step produces a quadratic equation for $\tilde{u}_z(1)$, with the two solutions $\tilde{u}_z(1) = [1 \pm \sqrt{1 - 4\Lambda\mathcal{I}(1, d/a)}]/2\Lambda$. The upper solution is in fact unstable, as we show next, but first we substitute the expression for the lower solution of $\tilde{u}_z(1)$ back into Eq. (6) to arrive at

$$\tilde{u}_z(\tilde{r}) = \frac{2}{1 + \sqrt{1 - 4\Lambda\,\mathcal{I}(1, \frac{d}{a})}}\mathcal{I}\left(\tilde{r}, \frac{d}{a}\right), \tag{7}$$

which gives the surface deformation in terms of only Λ and d/a.

To examine the stability of the deformed system, we reexpress the problem in terms of a minimization of energies rather than a balance of forces. The dominant contributions to the total energy of the system are (1) the elastic energy of the deformed substrate and (2) the reduction in energy that results from the droplet wetting the two solids. We neglect the energy of the liquid-gas interface since $h \ll a$, which is equivalent to neglecting the secondary curvature a^{-1} in the prior calculations.

For a given droplet volume V, we calculate the total energy U in terms of the deformed droplet radius a as

$$U = \frac{\pi E a h^2}{16(1-\nu^2)\mathcal{V}(\frac{d}{a})}\left[1-\left(\frac{a_s}{a}\right)^2\right] - 2\pi\gamma a^2, \qquad (8)$$

with the first term resulting from elastic contributions and the second resulting from wetting. Here, $a_s = \sqrt{V/\pi h}$ is the radius of a droplet of volume V in an undeformed geometry and $\mathcal{V}(d/a) = \int_0^1 \mathcal{I}(\tilde{r}, d/a)\tilde{r}d\tilde{r}$.

The nondimensional energy $\tilde{U} = U/[E^2h^4\pi/128\gamma(1-\nu^2)^2]$ is plotted in Fig. 2 against the drop radius Λ for various nondimensional drop volumes, $\Lambda_s = (8\ell_{EC}/h^2)\sqrt{V/\pi h}$. Note that Fig. 2 and the following analysis are for a substrate of infinite thickness, i.e., $d/a \to \infty$, but similar behavior occurs when the substrate is finite. For the smallest drop volume plotted, $\Lambda_s = 0.05$, we see that only one equilibrium state exists, corresponding to an energy minimum near the undeformed state of $\Lambda = \Lambda_s$. Then, as the drop volume increases, i.e., Λ increases, a second unstable equilibrium appears (see the curve for $\Lambda_s = 0.2$). This unstable equilibrium corresponds to the neglected negative root in Eq. (7). Finally, when $\Lambda_s = [(\pi-2)/2\pi]\sqrt{(8-\pi)/3\pi} \approx 0.261$, the minimum becomes a saddle point, and the gap collapses into a lower energy state corresponding to solid-solid contact.

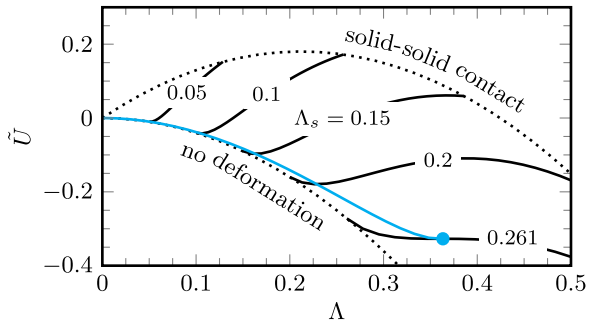

FIG. 2 (color online). Energy landscape for a droplet sandwiched between substrates of infinite thickness, $d/a \to \infty$. The solid black lines correspond to constant drop volumes Λ_s. They are bounded by the line of no deformation on the bottom ($a = a_s$ for $\tilde{U} = -\Lambda^2$) and solid-solid contact on the top [$u_z(0) = h/2$ for $\tilde{U} = (4/3\pi)\Lambda - \Lambda^2$]. The overlaid blue line denotes the equilibrium position and ends at the point of catastrophic collapse.

Surprisingly, the maximum deformation at the critical value of Λ_s is only $u_z(0)/h = (\pi-2)/4 \approx 0.285$, meaning that collapse is triggered when the gap is barely halfway closed. This abrupt collapse is not reversible; indeed, the problem exhibits significant hysteresis that depends on the interfacial energy for solid-solid contact. For the experimental conditions described below, we have observed that solid-solid contact, once initiated, is maintained after the drop of liquid evaporates completely. A similar bifurcation and pattern of hysteresis occurs in the elastocapillary adhesion of thin structures [17], and has been suggested for spheres [6].

We now present a series of experiments to test the predicted deformations. Our model experiment mimics the geometry of Fig. 1, with polydimethylsiloxane (PDMS) as the elastic material and a droplet of deionized water in the gap. The droplet is allowed to evaporate slowly so that a variety of different radii may be tested in identical experimental conditions. By varying the drop radius we change both nondimensional parameters, Λ and d/a.

The PDMS (Sylgard 184) is mixed in a base-to-curing-agent ratio of 10:1, 20:1, or 40:1 and baked at 70 °C until it is fully cured (time varies depending on the ratio). These recipes result in measured Young's moduli of $E = 1250 \pm 50$, 620 ± 30, 87 ± 4 kPa, respectively. The highest value is two orders of magnitude larger than that used to observe elastocapillary deformations in previous studies of sessile droplets [13–15]. The back side of the PDMS is plasma bonded to a rigid glass slide (1 mm thick) to achieve a zero-displacement boundary condition.

We use fluorescent beads (1.01 μm diameter, Bangs Laboratories) adsorbed to each PDMS surface to indicate the precise z location of the surfaces. To attach the beads, the substrate is first treated with oxygen plasma for 20 s, and then 1 mL of a 250:1 dilution of the stock bead solution is deposited before being aspirated off. PDMS is by default slightly hydrophobic, so the surface must be modified to alter its wetting characteristics. We follow the method of [24] to graft polyvinylpyrrolidone (PVP) polymer brushes to the surface of the PDMS, which results in a contact angle of $\theta_c \approx 4°$. A ring-shaped spacer (i.d. = 2 mm, Kapton film) is placed between the two pieces of PDMS to set a constant gap height. We use different thicknesses of Kapton film to adjust the gap height.

A 25–250 nL droplet of deionized water is placed in the gap between the two surfaces, and the assembly is viewed from below with an inverted confocal microscope (Leica TCS SP5). We measure the deformation as the droplet slowly evaporates. The vacated gap is then used as the reference state for the undeformed geometry. Using interferometry we obtain precise measurements of differences in gap height over large r distances, which are combined with

a high-magnification confocal z stack to give us the absolute gap height at a known reference point.

We report interferometry fringe patterns (2.5×, NA 0.25) in Fig. 3, which result from differences in gap height that cause either constructive or destructive interference [25]. Adjacent light bands (or dark bands) correspond to a difference in gap height of $\Delta h = \lambda/(2n)$, where $\lambda = 488$ nm is the wavelength of the light used and n is the refractive index of the material in the gap; $n = 1.00$ for air and $n = 1.33$ for water at our experimental conditions.

A 40× objective (NA 0.6) is used for the confocal z stack, with a stack taken before and after each interferometric image [see Figs. 3(a) and 3(b) for an indication of the location and relative size of this query region]. The fluorescent beads provide a precise indication of the absolute location of the top and bottom surfaces of the gap. The high magnification objective allows for a narrow depth of field, and hence precise z measurements.

We analyze the gap profile with a droplet present [Figs. 3(a) and 3(c)] and after the droplet has evaporated [Fig. 3(b)]. Note that the height of the vacant undeformed gap in Fig. 3(b) is not constant; if it were constant, we would not see the alternating fringes. We determine the gap profile along a line that intersects the center of the droplet [Fig. 3(a)] and along an identical line in the undeformed image [Fig. 3(b)]. We then subtract the profile of the deformed case from the undeformed case to obtain $2u_z(r)$.

The results provided in Fig. 4 show characteristic deformation profiles $u_z(r)$ for different droplet sizes in a given gap geometry ($h = 58.3 \pm 0.4$ μm and $d = 3.2 \pm 0.1$ mm). Given d and a, we have a prediction from Eq. (4) for the shape of the deformation, $\mathcal{I}(r/a, d/a)$. The shape can be expressed as

$$u_z\left(\frac{r}{a}\right) = u_z^m \mathcal{I}\left(\frac{r}{a}, \frac{d}{a}\right) + u_z^o, \tag{9}$$

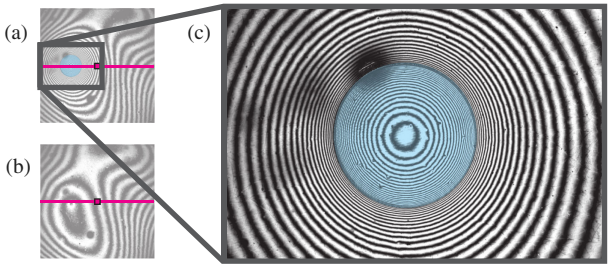

FIG. 3 (color online). Interferometric images (drop artificially colored blue). (a) The entire field of view. (b) The experiment after evaporation (images are 6.2 mm square). Pink lines indicate the profile queried for interferometry, and the small outlined squares indicate the size and shape of the confocal z-stack region. (c) A close-up of the droplet in (a) to emphasize the concentric rings. Droplet radius is $a = 586$ μm (image is 3.1 mm wide).

with a magnitude u_z^m and an offset u_z^o. We fit Eq. (9) to intersect the two data points outside of the droplet that are nearest and farthest from the contact line. As is evident in Fig. 4, the intermediate points fit the theoretical shape for a range of a (and hence d/a).

The data inside of the droplet require special treatment. There is an unknown jump in the deformation between the inside and the outside of the droplet, since the fringes beneath the circular meniscus are obscured by refraction. To estimate this jump, we specify that the deformation at the inner fringe closest to the meniscus is equal to the prediction from the fit to Eq. (9). The remaining inner points are offset by the same amount and follow the theory, as can be seen in Fig. 4.

Experimental u_z^m, determined from fitting to Eq. (9), are plotted against droplet radius a in the inset of Fig. 4. Included with these data are theoretical predictions from Eq. (7), $u_z^m = 8\ell_{\mathrm{EC}} a\, h^{-1}\left(1 + \sqrt{1 - \frac{32\ell_{\mathrm{EC}} a}{h^2}\mathcal{I}(1, d/a)}\right)^{-1}$, which are calculated from measured geometric and material parameters (a, h, d, E, ν, γ). The theoretical predictions for u_z^m match the measurements quite well for a wide range of experimental conditions, described in the caption of Fig. 4. The deviations from theory that do occur are likely due to variations in h or θ_c, difficulties in measuring E, or secondary curvature effects as $a \to h/2$. The offset u_z^o in Eq. (9) is due to the limited z-stack resolution

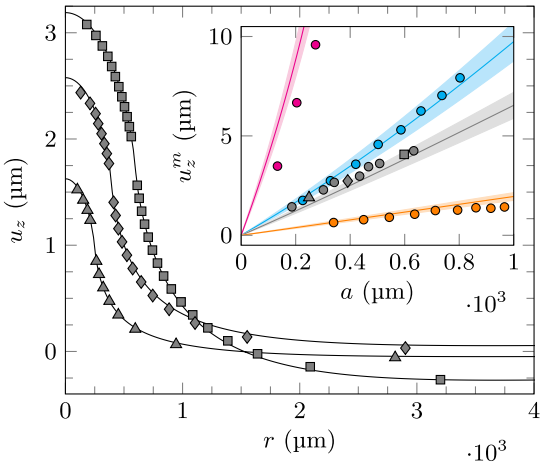

FIG. 4 (color online). Deformation for $a = 249$, 391, 598 μm. Experimental measurements are shown with symbols. The gap in the data corresponds to the unresolvable region beneath the meniscus. The solid lines denote the fit to Eq. (9) as described in the text. Inset: Deformation magnitude u_z^m plotted against droplet size a. 40:1 PDMS is used for the pink points, 20:1 for the blue and gray, and 10:1 for the orange. From top to bottom, $h = 66.4$, 43.8, 58.3, 89.5 ± 0.4 μm, and $d = 3.1$, 3.8, 3.2, 3.0 ± 0.1 mm. The colored lines denote the theoretical prediction, with their spread denoting uncertainty in geometric and material parameters. The noncircular gray points correspond to their counterparts in the main plot.

involved in determining the absolute deflection, and in all cases $|u_z^o| < 0.4$ μm.

As predicted by theory and proven with experiments, the geometry of a capillary bridge acts to magnify the deformation caused by capillary forces. This deformation, in turn, is expected to enhance the adhesion force through the mechanisms mentioned earlier: an increased drop radius and a decreased gap height. By applying these ideas to a variety of physical systems ranging from soft robotics [26] to the construction of granular structures [27], substrate softness may be used as a convenient tool to amplify the force of capillary adhesion.

The authors thank Camille Duprat, Bo Sun, Rob Style, Suzie Protiere, Janine Nunes, John Cannarella, and Jay Benziger for helpful discussions, and the NSF for support via Grant No. CBET-1132835.

*hastone@princeton.edu

[1] H.-J. Butt and M. Kappl, Adv. Colloid Interface Sci. **146**, 48 (2009).
[2] S. Herminghaus, Adv. Phys. **54**, 221 (2005).
[3] J. Qian and H. Gao, Acta Biomater. **2**, 51 (2006).
[4] K. L. Johnson, *Contact Mechanics* (Cambridge University Press, New York, 1985), 1st ed.
[5] A. Fogden and L. R. White, J. Colloid Interface Sci. **138**, 414 (1990).
[6] I. G. Goryacheva and Y. Y. Makhovskaya, J. Appl. Math. Mech. **65**, 273 (2001).
[7] H.-J. Butt, W. J. P. Barnes, A. del Campo, M. Kappl, and F. Schönfeld, Soft Matter **6**, 5930 (2010).
[8] B. Roman and J. Bico, J. Phys. Condens. Matter **22**, 493101 (2010).
[9] G. Lester, J. Colloid Sci. **16**, 315 (1961).
[10] A. I. Rusanov, J. Colloid Interface Sci. **63**, 330 (1978).
[11] S. Das, A. Marchand, B. Andreotti, and J. H. Snoeijer, Phys. Fluids **23**, 072006 (2011).
[12] R. W. Style and E. R. Dufresne, Soft Matter **8**, 7177 (2012).
[13] R. Pericet-Camara, A. Best, H.-J. Butt, and E. Bonaccurso, Langmuir **24**, 10565 (2008).
[14] E. R. Jerison, Y. Xu, L. A. Wilen, and E. R. Dufresne, Phys. Rev. Lett. **106**, 186103 (2011).
[15] R. W. Style, R. Boltyanskiy, Y. Che, J. S. Wettlaufer, L. A. Wilen, and E. R. Dufresne, Phys. Rev. Lett. **110**, 066103 (2013).
[16] W. Barnes, MRS Bull. **32**, 479 (2007).
[17] C. Mastrangelo, Tribol. Lett. **3**, 223 (1997).
[18] T. Gervais, J. El-Ali, A. Günther, and K. F. Jensen, Lab Chip **6**, 500 (2006).
[19] S. M. Wiederhorn, J. Am. Ceram. Soc. **50**, 407 (1967).
[20] A. Grimaldi, M. George, G. Pallares, C. Marlière, and M. Ciccotti, Phys. Rev. Lett. **100**, 165505 (2008).
[21] P. Howell, G. Kozyreff, and J. Ockendon, *Applied Solid Mechanics* (Cambridge University Press, Cambridge, England, 2009).
[22] The second radius of curvature is not exactly a, since a measures the radius of the contact line. However, for drops with $h \ll a$ the difference is a higher-order effect.
[23] Examination of Fig. 4 reveals that du_z/dr, and hence $d\tilde{u}_z/dr$, is steepest at the contact line, $\tilde{r} = 1$. In fact, for a substrate with infinite thickness, $d\mathcal{I}/dr$ is logarithmically singular at this point. The weak nature of this singularity, however, means that even large values of d/a produce $d\tilde{u}_z/d\tilde{r}$ that is of order 1. Furthermore, it is likely that local effects due to the contact line force and the surface tension of the solid will weaken the singularity [12].
[24] S. Hemmilä, J. V. Cauich-Rodríguez, J. Kreutzer, and P. Kallio, Appl. Surf. Sci. **258**, 9864 (2012).
[25] G. Wiegand, K. R. Neumaier, and E. Sackmann, Appl. Opt. **37**, 6892 (1998).
[26] R. F. Shepherd, F. Ilievski, W. Choi, S. A. Morin, A. A. Stokes, A. D. Mazzeo, X. Chen, M. Wang, and G. M. Whitesides, Proc. Natl. Acad. Sci. U.S.A. **108**, 20400 (2011).
[27] M. Pakpour, M. Habibi, P. Møller, and D. Bonn, Sci. Rep. **2**, 549 (2012).